



TiNbCr Multi-Principal Element Alloy Oxidation Behavior in Air at 800–1000 °C

Isabela Dainezi^{1,2} · Brian Gleeson³ · Bruno Resende Buzatti⁴ ·
Artur Mariano de Sousa Malafaia⁴ · Carlos Alberto Della Rovere^{1,2}

Received: 22 February 2024 / Revised: 8 April 2024 / Accepted: 11 April 2024 /
Published online: 29 April 2024

© The Author(s), under exclusive licence to Springer Science+Business Media, LLC, part of Springer Nature 2024

Abstract

The isothermal and cyclic oxidation behavior of a multi-principal element (MPE) TiNbCr alloy at 800–1000 °C in air was studied and compared to Co-based alloy 188. The phase constitution of the MPE alloy consisted of a Nb-rich body-centered cubic (BCC) matrix and Cr-rich Laves precipitates. While isothermal tests conducted at 800 °C led to the formation of a complex mixture of Nb, Ti and Cr oxides, tests at 900 and 1000 °C resulted in the formation of an innermost Cr₂O₃-rich scale layer which provided improved oxidation resistance. However, for all exposure temperatures, the scaling kinetics of the alloy were linear and therefore deemed non-protective. In contrast, alloy 188 exhibited parabolic scaling kinetics and smaller mass gain per area than the MPE alloy. The similarity between isothermal and cyclic test results for the MPE alloy confirmed that the scale does not offer much protection. Additionally, for all tests, there was extensive internal oxidation and nitridation.

Keywords Multi-principal element alloy · Refractory metals · Oxidation · Growth kinetics · Scale microstructure

✉ Isabela Dainezi
beladainezi@gmail.com

✉ Carlos Alberto Della Rovere
rovere@ufscar.br

¹ Graduate Program in Materials Science and Engineering, Federal University of Sao Carlos, Rodovia Washington Luiz, km 235 SP-310, São Carlos, São Paulo 13565-905, Brazil

² Department of Materials Engineering, Federal University of Sao Carlos, Rodovia Washington Luiz, km 235 SP-310, São Carlos, São Paulo 13565-905, Brazil

³ Department of Mechanical Engineering and Materials Science, University of Pittsburgh, Pittsburgh, PA 15261, USA

⁴ Mechanical and Industrial Engineering Department, Federal University of São João del-Rei (UFSJ), Praça Frei Orlando, 170, Centro, São João del-Rei, Minas Gerais, Brazil

Introduction

Studies on multi-principal element (MPE) alloys have been increasingly reported in recent years, but those aimed at high-temperature oxidation behavior are still very recent and little explored. As highlighted by Birbilis and colleagues [1], achieving environmental resistance for MPE systems is still a challenge. Even so, MPE alloys based on refractory metals have potential to replace conventional alloys in some applications, such as the replacement of nickel-based superalloys used in aero-turbine engines.

Miracle and Senkov [2] reported that additions of Al, Cr, Ti and Si tend to increase the oxidation resistance of MPE alloys, while the addition of V reduces it. The addition of Al also leads to a reduction in the density of the alloy, as does the addition of Ti, but the formation of binary or ternary intermetallic phases may occur. This may be avoided by reducing the amount of Cr in the alloy [3–6], together with balanced composition control.

Previous work on MPE alloys based on refractory metals has generally found that the formation of a protective aluminum and chromium oxides (Al_2O_3 and Cr_2O_3) rarely occurs, since these have very slow formation kinetics relative to the oxides of the principal constituents [2, 7–10]. Even so, mixed oxides such as NbCrO_4 may form and can impart slower oxidation kinetics than conventional refractory alloys [6, 11–14].

Comparing the oxidation behavior of MPE alloys with refractory elements to refractory commercial alloys, Gorr and colleagues [8] deduced that mixed-oxide formation may reduce the oxidation kinetics, as noted for NbCrO_4 , NbTiO_4 and TiNb_2O_7 compared to pure Nb oxides. To that end, Gorr and colleagues [8] showed that MPE alloys containing Ta, Nb, Ti, Cr, Al and Si are among promising refractory alloys resistant to oxidation. In agreement with this, Butler and colleagues [15] found that the 24-h oxidation kinetics of NbCr and TiNbCr alloys at 1200 °C in air were similar and almost parabolic (over the entire exposure period), whereas the kinetics of a TaTiNbCr alloy were lower and showed parabolic behavior only up to 8 h, but then linear thereafter. It was reported by that research group that the linear kinetics were associated with scale spallation and mixed-oxide-scale formation in the form of repetitive and non-continuous layers that had a high amount of pores and cracks.

Butler and colleagues [16] also characterized these NbCr-based MPE alloys and verified that: (i) the microstructure of the NbCr alloy consists of a Laves phase matrix (C15) and BCC phase precipitates; (ii) the addition of Ti to the NbCr alloy inverts the microstructure to a predominantly BCC matrix (rich in Ti) with Laves precipitates; and (iii) the addition of Ta to the ternary alloy (TiNbCr) can increase the volumetric fraction of the BCC matrix and retain the precipitation of the Laves phase.

Welch and colleagues [17] studied the oxidation behavior of TaTiCr-based MPE alloys in air at 1200 °C up to 24 h. Differently from that observed by Butler and colleagues [15], the former researchers did not observe parabolic scaling kinetics behavior. Instead, they observed that: (i) the TaTiCr MPE alloy had the slowest

kinetics that exhibited near-cubic behavior, with the scale characterized as a coherent and layered scale composed of a TiO_2 outer layer, followed by Cr_2O_3 and mixed rutile-structured oxides and then an extended internal reaction zone; (ii) the second-best performer was a Ta_4TiCr_3 MPE alloy and it exhibited three different kinetics regimes, i.e., near-parabolic up to 9 h, linear from 9 to 16 h and a higher-rate linear behavior from 16 to 24 h, all attributed to oxide rumpling, cracking and subsequent internal oxidation; and (iii) the Ta_2TiCr and $\text{Ta}_4\text{Ti}_3\text{Cr}$ MPE alloys exhibited near-linear kinetics and formed thick, porous oxides that showed severe cracking.

Studies on the oxidation behavior of MPE alloys, as outlined by Gorr et al. [8], have predominantly focused on high-temperature isothermal conditions. However, it is important to assess different temperature regimes, which may reveal distinct mechanisms and phenomena, including enhanced oxidation (e.g., pesting) at low temperatures and oxide volatilization at higher temperatures. Additionally, it is important to understand the oxidation behavior of these alloys exposed to thermal cycling conditions.

In this context, the present study was conducted with the aim of investigating the TiNbCr MPE alloy oxidation behavior in air over a range of temperatures lower than previously reported. Specifically, the alloys were processed by HIP and casting and then isothermally oxidized at 800, 900 and 1000 °C for 20, 60 and 100 h in air. For comparison, cyclic oxidation testing in air was also conducted at 800 and 900 °C.

Experimental Procedures

The TiNbCr MPE alloy was first cast by vacuum-arc melting using high purity constituents (99.95%); the melting atmosphere was oxygen-gettered by initially melting high-purity Ti. A given alloy casting was flipped and re-melted several times to ensure chemical uniformity. Some samples were studied in the as-cast condition and others were hot isostatic pressed (HIP) at 1400 °C for 3 h using a pressure of 207 MPa after casting, with heating and cooling rates of 15 °C/min. In this study, both types of samples were not subjected to any heat treatment.

For oxidation tests, both as-cast and HIPed TiNbCr MPE coupon samples with approximate dimensions of $5 \times 5 \times 2$ mm were cut, drilled with a hole diameter of 1.5 mm, surface-abraded using SiC grinding pads up to a 1200-grit finish and then ultrasonic cleaned in ethanol. Isothermal oxidation tests in air were conducted using a tube furnace. Exposures were at 800, 900 and 1000 °C for 20, 60 and 100 h. Test specimens suspended by Kanthal (FeCrAl alloy) wires above alumina crucibles were inserted into the hot zone of the pre-heated furnace kept in place throughout the test duration. At the completion of a given test, the samples were removed and cooled naturally in air.

Cyclic tests were conducted using a WT Industry automatic furnace with software to control insertion and removal of the test samples. Only the HIPed TiNbCr MPE alloy was tested at 800 and 900 °C to 100 cycles of 60-min exposure and 10 min at room temperature. Additionally, due to the observed spallation at 900 °C, a specimen was suspended above a crucible to collect as much spallation as possible.

To provide a comparison of the isothermal oxidation behavior of the TiNbCr MPE alloy to a commercial system, alloy 188 specimens were also tested. The alloy 188 specimens were prepared in the same way as the TiNbCr MPE specimens. The compositions of the alloys tested are shown in Table 1. The TiNbCr composition is an average of at least three EDS measurements of relatively large areas, and alloy 188 is the nominal composition.

The topography and cross sections of the oxidized specimens were analyzed using an FEI Apreo scanning electron microscope (SEM) with EDAX EBSD and Octane Elite EDS Inspect S50 or a ZEISS Sigma 500 VP SEM with Oxford Aztec X-EDS. X-ray diffraction (XRD) analyses were performed using a Bruker D8 XRD system with copper-K α radiation and in the 2θ range of 25°–90° and a step of 0.5° for 2 s/step and analyzed using the software packages Search-Match and GSAS-II, enabling the identification of the phases. Cross-sectional mounts were prepared using standard metallographic procedures.

Results

The microstructure of the TiNbCr MPE alloy in each processed condition is shown in Fig. 1. Each microstructure was found to consist of a BCC matrix (Points 2 and 4) rich in Nb and Ti with Laves phase (Points 1 and 3) rich in Cr. The EDS measured phase compositions are presented in Table 2. Comparing Fig. 1a and b, it is of note that in the as-cast condition, the Laves phase is dispersed in the dendritic structure to the extent that it was not possible to distinguish BCC and Laves phase, as in the HIPed condition, and Nb segregated to the interdendritic areas. Additionally, it was found by Rietveld analysis of the XRD spectra that the HIPed TiNbCr MPE alloy has a higher Laves phase fraction, which is inferred to be due to the high temperature processing applied during HIPing.

Isothermal Oxidation Tests

Linear and logarithmic plots of the oxidation kinetics obtained at each test temperature for each alloy are shown in Fig. 2a–c. The TiNbCr MPE alloy exhibited similar kinetics in both processed conditions, with a higher mass gain per area at lower temperatures, suggesting a different scaling mechanism at different temperatures. However, it exhibited overall higher mass gains compared to alloy 188. Additionally, alloy 188, consistently, showed an increase in mass gain per area with the increase in test temperature (Fig. 2b), suggesting the same scaling mechanism. It should be noted that the total mass gain considered in these plots is the combination of oxidation, nitridation and spallation, as will be presented later.

A general growth-rate law was used to analyze the kinetics according to Eq. (1), in which ΔW is the mass gain (mg), A is the initial surface area (cm²), k is the rate constant, t is oxidation time and n is the time exponent. Oxidation kinetics characterized by $n = 1$ are linear, with the rate constrained by reaction occurring at the scale-gas and/or metal-oxide interface. At $n = 0.5$, the scale grows according

Table 1 Chemical composition of the studied alloys in atomic percentage (at.%)

Alloy	B	C	Co	Cr	Fe	La	Mn	Nb	Ni	Si	Ti	W	O
TiNbCr*	–	–	–	33.7 ± 1.3	–	–	–	31.7 ± 1.3	–	–	29.8 ± 2.2	–	4.9 ± 1.4
alloy 188**	0.015 max	0.10	39 Bal	22	3 max	0.03	1.25 max	–	22	0.35	–	14	–

*Average from three or more EDS measurements of each condition

**Nominal chemical composition from: Haynes International—HAYNES® 188 alloy [18]

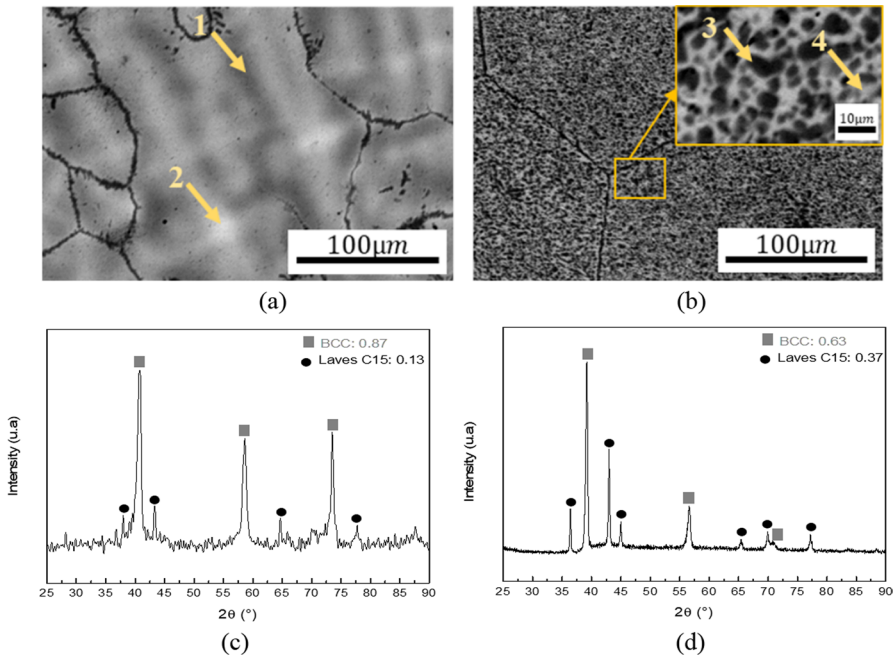


Fig. 1 SEM images of TiNbCr MPE alloy in condition **a** as-cast and **b** HIPed, with EDS areas indicated and XRD spectra in condition **c** as-cast and **d** HIPed

Table 2 EDS analysis (at.%) results for points shown in Fig. 1a and b

at.%	Cr	Nb	Ti	O
1	31.4 ± 2.1	28.3 ± 1.6	33.3 ± 0.2	6.7 ± 0.3
2	30.5 ± 0.7	32.4 ± 2.1	30.9 ± 1.9	6.3 ± 0.1
3	59.7 ± 0.8	21.2 ± 0.2	18.9 ± 0.6	0.2 ± 0.1
4	14.7 ± 0.8	35.2 ± 0.4	37.4 ± 0.9	12.7 ± 1.4

to parabolic kinetics, indicating a diffusion-controlled growth process through the growing scale. Exponents ranging between 1 and 0.5 suggest a mixed-mode behavior, involving both diffusion- and interface-controlled mechanisms. Kinetics exhibiting sub-parabolic behavior below 0.5 indicate diffusion-controlled reactions perhaps combined with volatilization effects, as seen in cubic kinetics with $n = 0.3$ [17]. The results for the current tests are shown in Table 3.

$$\ln \left(\frac{\Delta W}{A} \right) = \ln k + n \ln t \quad (1)$$

Referring to Table 3, it becomes evident that at 800 °C, the TiNbCr MPE alloy displays an approximately linear kinetic behavior, as indicated by the time exponent close to 1. However, as the temperature increases, this exponent lies within the range of 0.5–1, indicating mixed-mode behavior involving both diffusion and

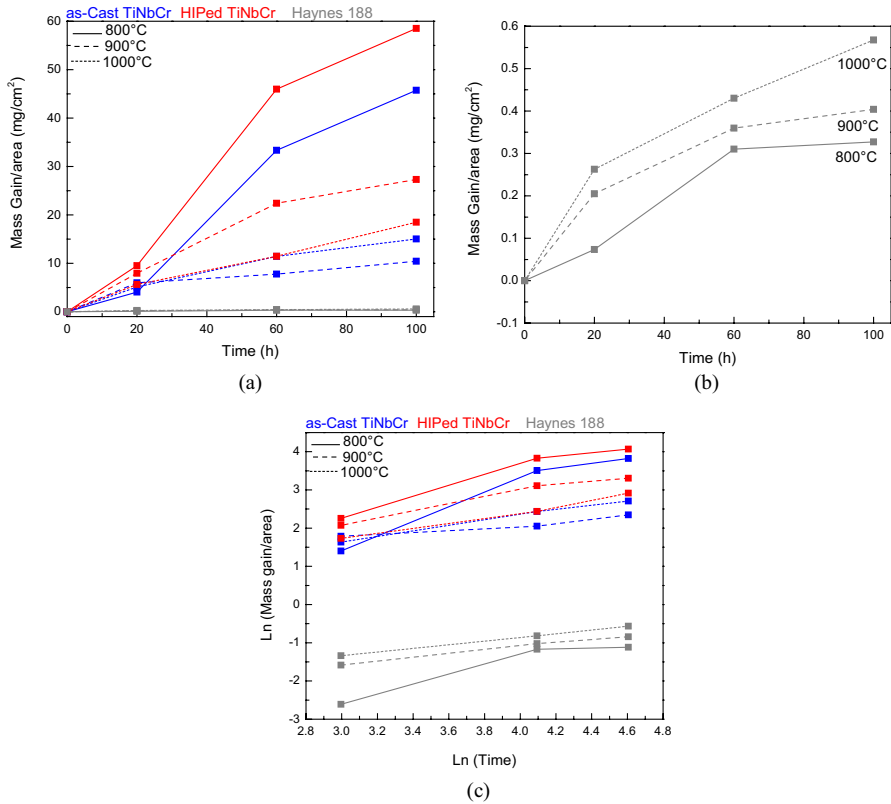


Fig. 2 Comparison of mass change per area for TiNbCr MPE alloy and alloy 188 at 800, 900 and 1000 °C during isothermal oxidation in air represented in: **a** linear plot, **b** for alloy 188 only, and **c** a comparison in natural logarithmic plot

Table 3 Reaction rate constants (*k*) and time exponents (*n*) for TiNbCr MPE and alloy 188 at 800, 900 and 1000 °C

Alloy	Temperature (°C)	<i>n</i>	<i>R</i> ²	$k \left(\frac{g}{cm^2 \cdot s^n} \right)$
As-Cast TiNbCr	800	1.07	0.95	2.02×10^{-8}
	900	0.83	0.93	1.16×10^{-5}
	1000	0.67	0.98	2.35×10^{-6}
HIPed TiNbCr	800	1.09	0.92	4.78×10^{-8}
	900	0.79	0.88	1.11×10^{-6}
	1000	0.62	0.99	3.34×10^{-6}
Alloy 188	800	0.88	0.84	2.89×10^{-9}
	900	0.46	0.99	4.02×10^{-8}
	1000	0.47	0.99	6.47×10^{-8}

reaction-controlled mechanisms, a pattern similar to that observed in alloy 188 at 800 °C. This finding for TiNbCr MPE alloy suggests a transition in the oxidation mechanism with an increase in temperature.

Representative topography images by optical microscopy (OM) and SEM of all alloys after 100-h oxidation at 800, 900 and 1000 °C are shown in Figs. 3, 4, 5 and 6. Oxide identification was based on EDS analysis and supported by XRD (Fig. 7). Due to the similarity between the as-cast and HIPed TiNbCr MPE alloy, only OM images for the as-cast are shown in Fig. 3 and the XRD in Fig. 7.

Figure 3 highlights that spallation areas were present for the as-cast TiNbCr MPE alloy after all exposure temperatures, with more severe spallation observed in the sample tested at 800 °C. This suggests that the mechanism at 800 °C offers reduced protection compared to 900 and 1000 °C, as also indicated in Fig. 2a with the higher value for the mass gain per area for the as-cast TiNbCr.

Comparing Figs. 4, 5 and 6, it is seen that alloy 188 forms denser external oxides scale than the two types of TiNbCr MPE alloy. The oxide scales on the MPE alloys

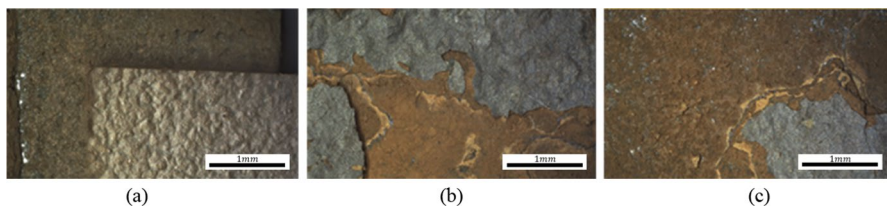


Fig. 3 OM topography images of as-cast TiNbCr MPE alloy after 100-h test in air at **a** 800 °C, **b** 900 °C and **c** 1000 °C

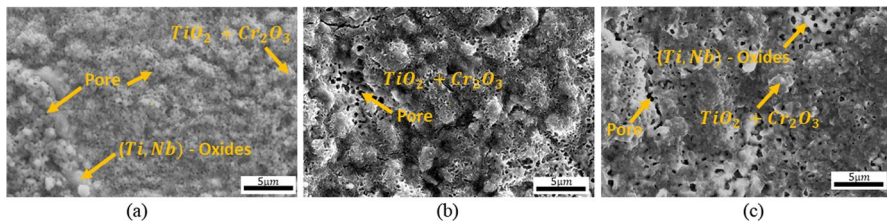


Fig. 4 SEM topography images of as-cast TiNbCr MPE alloy after 100-h test in air at **a** 800 °C, **b** 900 °C and **c** 1000 °C

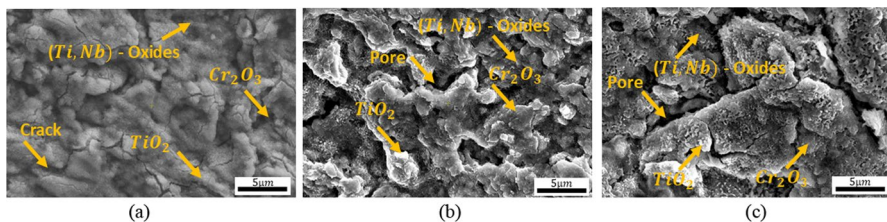


Fig. 5 SEM topography images of HIPed TiNbCr MPE alloy after 100-h test in air at **a** 800 °C, **b** 900 °C and **c** 1000 °C

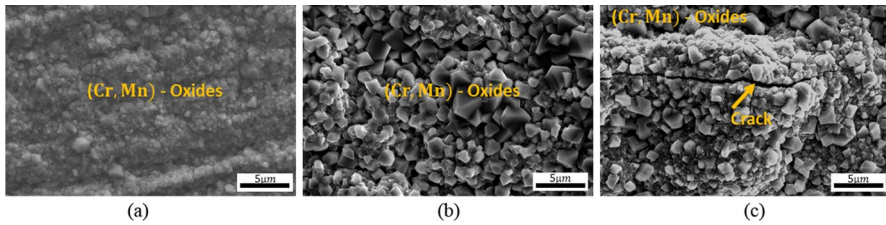


Fig. 6 SEM topography images of alloy 188 after 100-h test in air at **a** 800 °C, **b** 900 °C and **c** 1000 °C

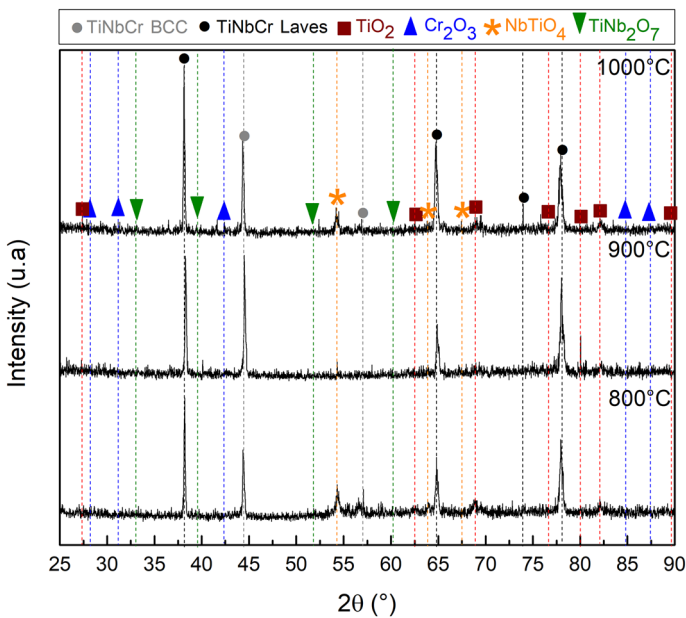


Fig. 7 XRD spectra from as-cast TiNbCr MPE alloy after 100-h oxidation in air at the indicated temperatures

are characterized by a higher density of pores than the scales on the alloy 188. The presence of porosity enables gas ingress through the scale and may detrimentally affect overall protection, as indicated by the higher weight gains in Fig. 2a. Additionally, an increase in temperature generated higher porosity.

Representative cross-sectional SEM images of the oxidized samples are presented in Figs. 8, 9 and 10. The inferred oxides, based on EDS and XRD analyses, are indicated in each image. It is of note that on the TiNbCr MPE alloy a clearly non-protective and non-adherent oxide scale is formed at all temperatures, suggesting linear kinetics, regardless of processing route. Additionally, even though the time exponent obtained from Fig. 2 and shown in Table 3 suggests a mixed-mode behavior, there is a predominant appearance that would be associated with linear behavior. The oxide product has a stratified porous layer morphology and an internal reaction zone.

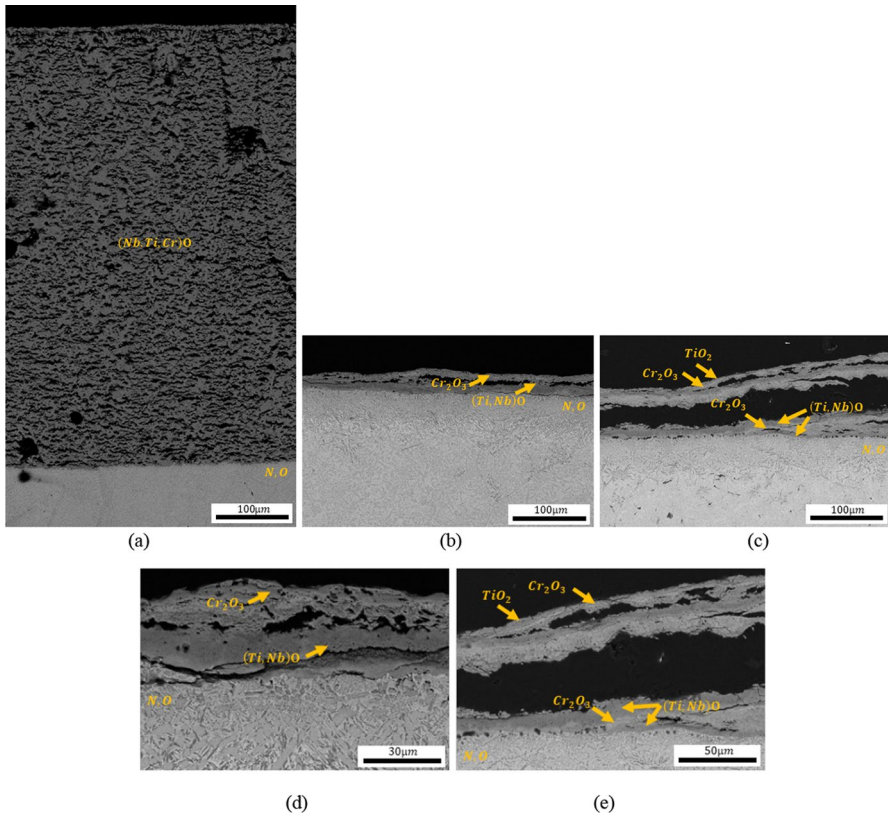


Fig. 8 Cross-sectional SEM images of as-cast TiNbCr MPE alloy after 100-h test in air at **a** 800 °C, **b** 900 °C and **c** 1000 °C. Detailed SEM images of as-cast TiNbCr MPE alloy after 100 h in air at **d** 900 °C and **e** 1000 °C

By contrast, looking at the alloy 188 it is noted that a thin and adherent oxide layer with no evidence of an internal reaction zone formed at all temperatures studied. This fact suggests a parabolic behavior, even at 800 °C which is in agreement with the results of Herchenroeder and Deodeshmukh and colleagues [19, 20]. The time exponent in Table 3 suggests a mixed mode behavior, but this may be due to the limited resolution when using log–log plots to determine kinetic exponents.

Figures 11, 12 and 13 present element maps of the oxide scales formed on the as-cast TiNbCr MPE alloy after 20 h of testing at 800, 900 and 1000 °C in air, respectively. Due to the similarity between the as-cast and HIPed TiNbCr MPE alloy, only the as-cast condition is shown. Furthermore, as mentioned previously, for all tested conditions, the oxide scale spalled, and this spalling increased with testing time. Therefore, only the 20-h map is included. It is seen that at 800 °C the oxide scale is composed of a mixture of Nb, Ti and Cr oxides; however, increasing temperature to 900 °C causes Cr-rich oxide layers to form which, in

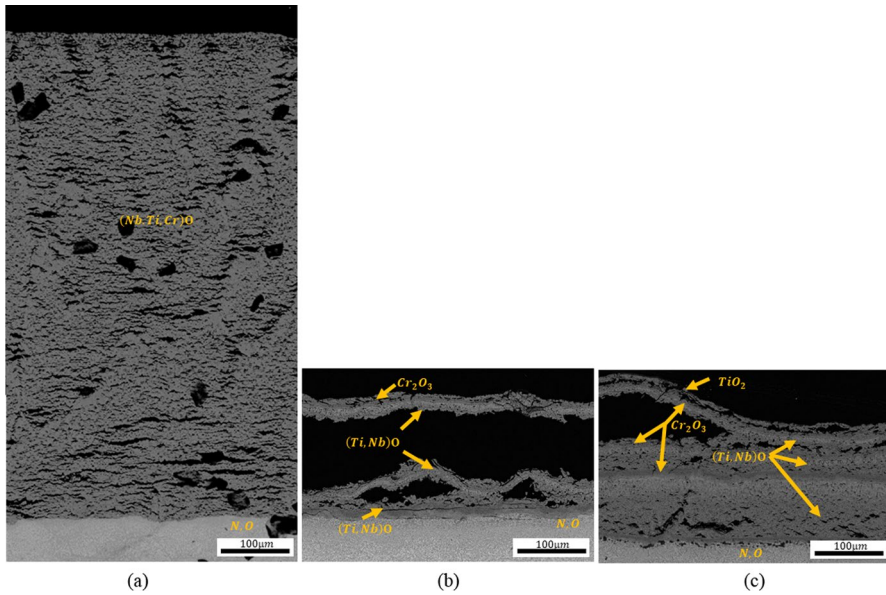


Fig. 9 Cross-sectional SEM images of HIPed TiNbCr MPE alloy after 100-h test in air at **a** 800 °C, **b** 900 °C and **c** 1000 °C

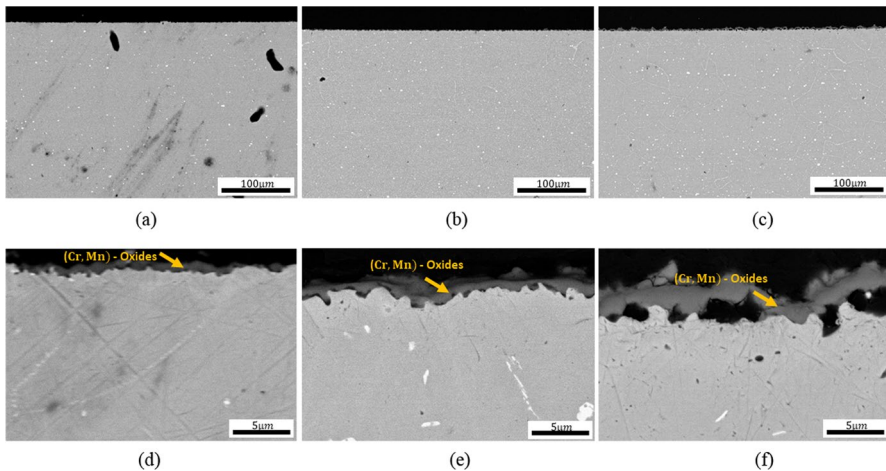


Fig. 10 Cross-sectional SEM images of alloy 188 after 100-h test in air at **a** 800 °C, **b** 900 °C and **c** 1000 °C. Detailed SEM images of alloy 188 after 100 h in air at **d** 800 °C, **e** 900 °C and **f** 1000 °C

accordance with the XRD results in Fig. 8, is deduced to be Cr_2O_3 . Additionally, at 1000 °C a Ti-rich oxide is observed as the most external layer. This layer was confirmed by XRD to be TiO_2 .

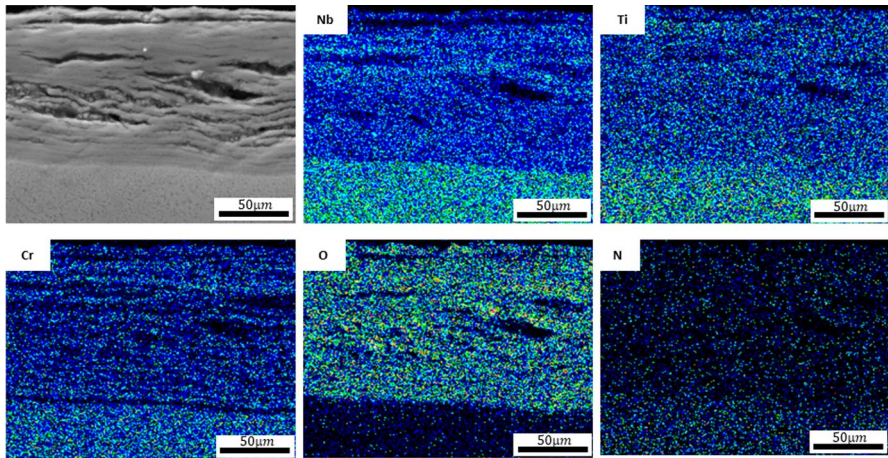


Fig. 11 EDS maps of cross section of as-cast TiNbCr MPE alloy after 800 °C isothermal oxidation in air for 20 h

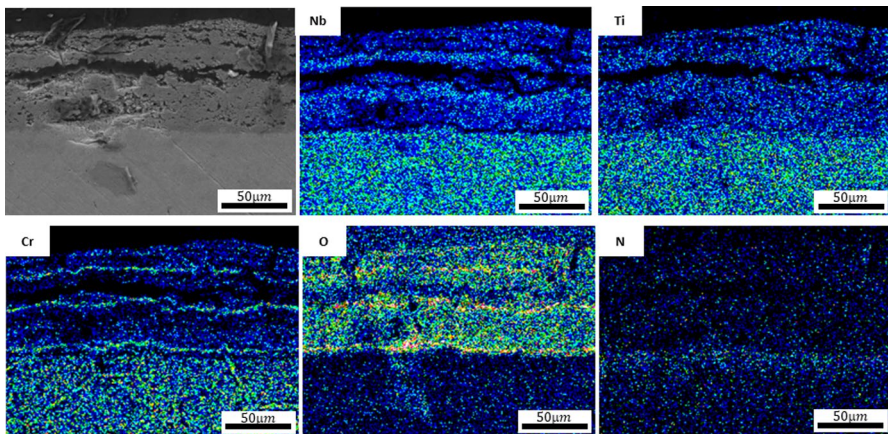


Fig. 12 EDS maps of cross section of as-cast TiNbCr MPE alloy after 900 °C isothermal oxidation in air for 20 h

More detailed EDS compositional analyses are presented in Figs. 14 and 15, with corresponding compositions in Tables 4 and 5, respectively. At 800 °C (Fig. 14), three regions were identified: A—external, B—intermediate, and C—interface between the scale and metal surface. Within these regions, three areas were chosen, and their compositional averages are presented in Table 4. As indicated in Fig. 11, the scale is composed of a mixture of Nb, Ti and Cr oxides with no defined layers.

By contrast, at 900 °C (and also at 1000 °C) (Figs. 12 and 13), an external Ti-rich layer formed followed by a Cr-rich oxide layer that is intermixed with layers

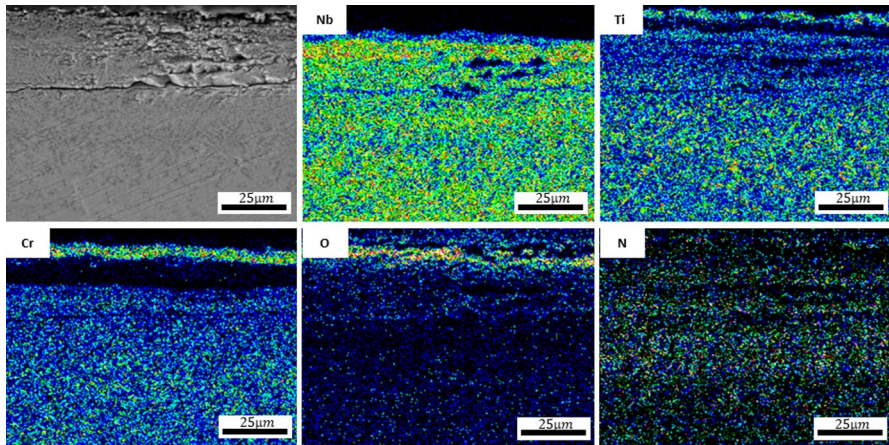


Fig. 13 EDS maps of cross section of as-cast TiNbCr MPE alloy after 1000 °C isothermal oxidation in air for 20 h

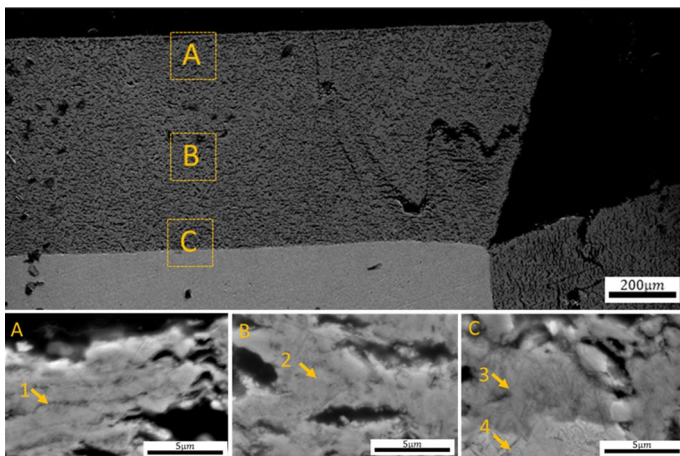


Fig. 14 SEM cross section of HIPed TiNbCr MPE alloy after 800 °C isothermal oxidation in air for 100 h with EDS areas shown by the numbers in the images

rich in Ti and Nb. According to XRD results, this inner structure is comprised of TiO_2 , Cr_2O_3 and the complex oxides NbTiO_4 and TiNb_2O_7 .

Additionally, Fig. 15 shows the presence of an internal reaction zone. As indicated in Table 5, this zone contains nitrides and oxides. The Laves phase contains oxides (point 2) and its boundary is rich in nitrogen (point 1). On the other hand, the BCC phase of the alloy is rich in oxygen, nitrogen, Nb and Ti (point 3), with some precipitates rich in these elements (point 4).

Moreover, according to Table 3, the TiNbCr MPE alloy demonstrates linear behavior at 800 °C and a mixed behavior at 900 and 1000 °C. However,

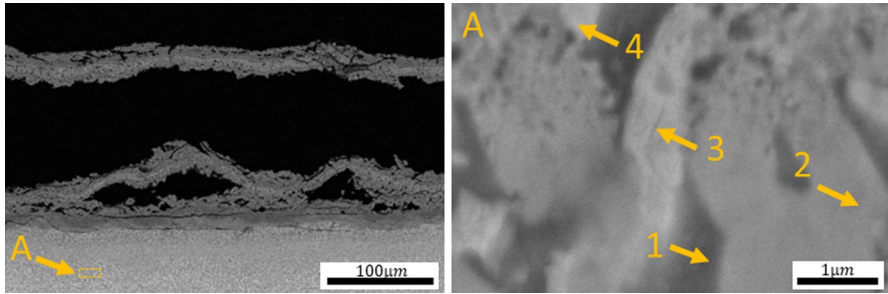


Fig. 15 SEM of cross section of HIPed TiNbCr MPE Alloy after 900 °C isothermal test in air during 100 h with EDS areas shown by the numbers in the image

Table 4 EDS analysis (at.%) results for areas shown in Fig. 14

Composition at.%	Cr	Nb	Ti	N	O
1	9.3 ± 1.7	9.5 ± 1.7	11.5 ± 1.2	0.00 ± 0.00	69.7 ± 2.3
2	8.3 ± 3.8	10.5 ± 1.1	11.9 ± 1.6	0.00 ± 0.00	69.4 ± 0.8
3	8.8 ± 2.9	10.7 ± 2.3	10.0 ± 2.4	0.00 ± 0.00	70.5 ± 1.8
4	3.3 ± 2.8	23.9 ± 1.7	24.9 ± 1.4	25.8 ± 3.8	22.1 ± 9.7

Table 5 EDS analysis (at.%) results for areas shown in Fig. 15

Composition at.%	Cr	Nb	Ti	N	O
1	9.3 ± 1.7	9.5 ± 1.7	11.5 ± 1.2	0.00 ± 0.00	69.7 ± 2.3
2	8.3 ± 3.8	10.5 ± 1.1	11.9 ± 1.6	0.00 ± 0.00	69.4 ± 0.8
3	8.8 ± 2.9	10.7 ± 2.3	10.0 ± 2.4	0.00 ± 0.00	70.5 ± 1.8
4	3.3 ± 2.8	23.9 ± 1.7	24.9 ± 1.4	25.8 ± 3.8	22.1 ± 9.7

cross-sectional analysis (Figs. 8 and 9) suggests from the preponderance of cracks and voids that the kinetics should be linear.

Based on EDS analysis, the penetration of oxygen and nitrogen to form the internal reaction zone (IRZ) was determined. All test conditions generated an IRZ with the associated kinetics compared in Fig. 16. An increase in exposure temperature generated an increase in the IRZ depth. Additionally, Fig. 16 shows that the IRZ depth in the HIPed samples is consistently deeper than as-cast samples, suggesting the detrimental behavior of the Laves-phase size and fraction, as will be discussed later.

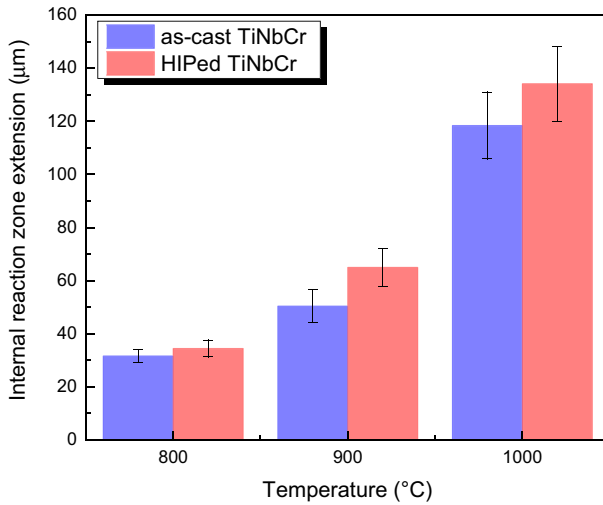


Fig. 16 Comparison based on cross section SEM analysis of internal reaction zones after 100-h testing

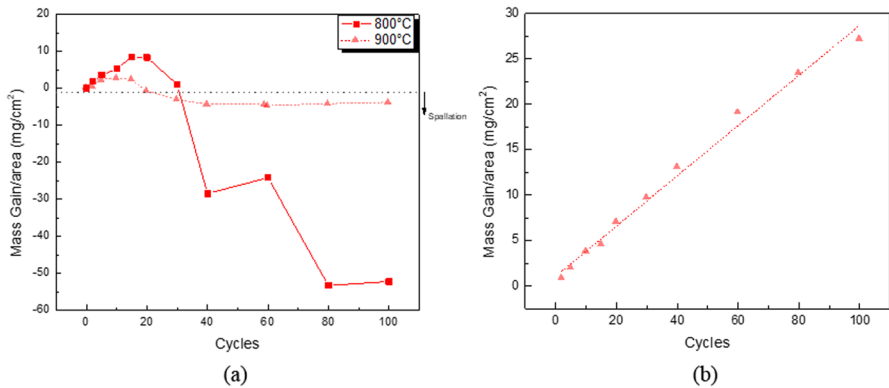


Fig. 17 Mass gain normalized by initial surface area in function of number of cycles for HIPed TiNbCr MPE Alloy testes at 800 and 900 °C. **a** Mass gain of sample with no collected spallation and **b** mass gain of sample plus collected spallation for the 900 °C exposure

Cyclic Oxidation

The mass gain per area as a function of the number of thermal cycles from 800 and 900 °C for the TiNbCr MPE alloy in the HIPed condition and with no spallation collected is shown in Fig. 17a. The results for the same test at 900 °C but with spallation collected are shown in Fig. 17b. After 15 cycles at 800 °C, the amount of spallation increased as shown in Fig. 17a. Linear kinetics at 800 °C can be fitted from the first to the 15th cycle, with the rate constant found to be $k_l = 1.38 \times 10^{-7} \frac{g}{cm^2 \cdot s}$. In the case of samples tested at 900 °C, linear kinetics can also be fitted, as indicated in Fig. 17b, with a rate constant of $k_l = 7.7 \times 10^{-8} \frac{g}{cm^2 \cdot s}$ calculated and a R^2 of 0.99. A

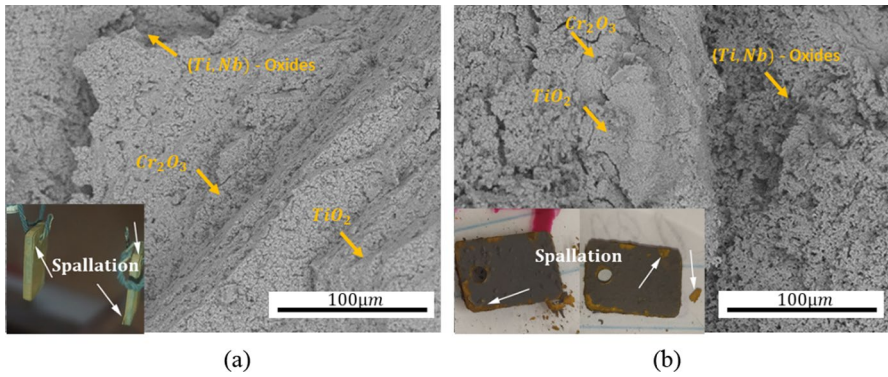


Fig. 18 Topography section of HIPed TiNbCr MPE alloy samples test in air after 100 cycles at **a** 800 °C and **b** 900 °C

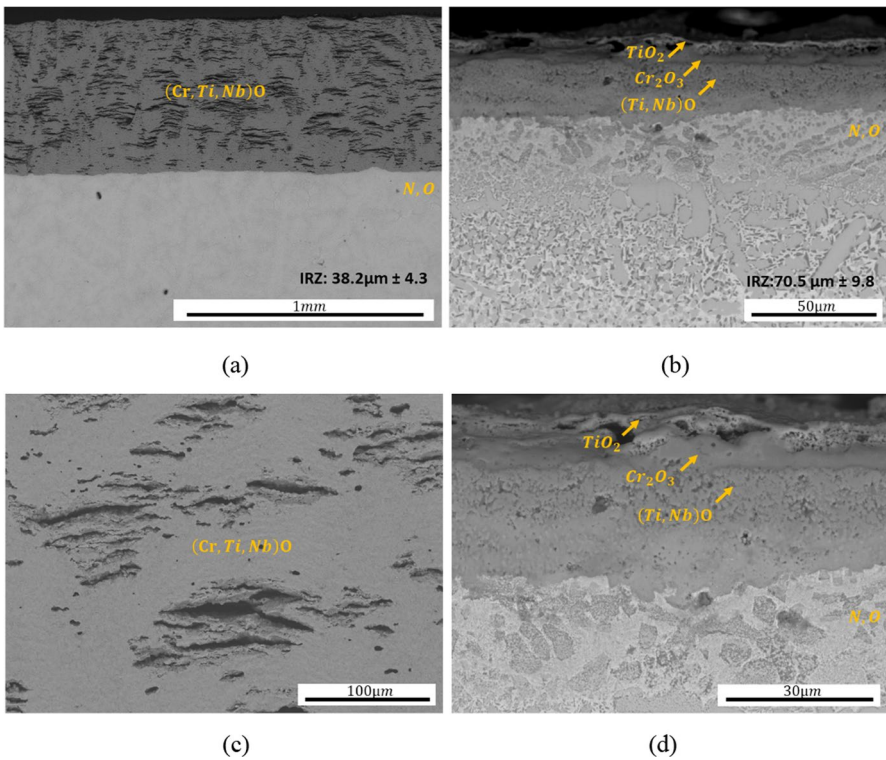


Fig. 19 Cross-sectional SEM images of HIPed TiNbCr MPE alloy after 100 cycles test in air at **a** 800 °C and **b** 900 °C. Detailed SEM images of HIPed TiNbCr MPE alloy after 100 cycles test in air at **c** 800 °C and **d** 900 °C

similar 900 °C rate constant was determined for the case when scale spallation was not collected (Fig. 17b). The 900 °C rate constants obtained from the cyclic tests were similar to the linear rate constant obtained from the 900 °C isothermal test (Table 3). This suggests that the scale was fairly tenacious but still nonprotective due to its growth rate being linear.

Representative topography and cross-sectional SEM images from the samples cyclic oxidized at 800 and 900 °C for 100 cycles are shown in Figs. 18 and 19, respectively. Due to the cyclic testing, the samples experienced tensile and compressive stresses from thermal expansions, resulting in oxide layer spallation with each cycle. The depicted images illustrate the samples' condition after 100 cycles, reflecting the cumulative impact of oxide layer formation and spallation over this duration. Similar observations to the samples oxidized isothermally can be found. However, the cross section of the HIPed TiNbCr MPE alloy isothermally oxidized for 100 h at 900 °C (Fig. 9) shows more Cr₂O₃ layers and complex (Ti,Nb) oxide layers in the scale than the scale product formed on the alloy cyclically oxidized (100 cycles total of 60 min at 900 °C for each) (Fig. 19b). This may be due to scale damage incurred during thermal cycling, but it was not further investigated.

At both 800 and 900 °C, the internal reaction zone thickness for samples tested isothermally and cyclically has similar values (Fig. 19), suggesting similar scaling behavior. However, the scale thickness has different values presumably due to scale damage incurred during thermal cycling.

Discussion

The TiNbCr MPE alloys in this work had the same composition (equimolar element amounts) and the same phase constitution, i.e., a combination of a BCC matrix rich in Nb and Ti and Laves-phase precipitates rich in Cr (Table 2). As characterized by Butler and colleagues [16] Laves phase results from a eutectic-like reaction to form BCC and Laves C14 during cooling ($Liq \leftrightarrow BCC + LavesC14$) [16]. The Ti enrichment in the BCC is due to Ti acting as a BCC stabilizer in refractory systems, while Cr acts as a Laves stabilizer, as characterized by Butler and colleagues [15, 16] for the same alloy processed by HIP under the same conditions.

However, comparing Fig. 1a and b, there is a difference between the TiNbCr structure processed by the two processing methods studied. The as-cast structure is dendritic and, according to the EDS and XRD analyses, it is comprised of Nb, Ti- rich BCC dendrites with fine (Nb, Ti)Cr₂ Laves precipitates in the interdendritic regions and along grain boundaries (Fig. 1a). In contrast, after the homogenization promoted by the HIP process, the dendritic structure in the alloy's metallic matrix transforms into a uniform BCC structure, and the fine Laves precipitates observed after casting coalesce into blocky, polygonal particles, located both along grain boundaries and within the grains. Similar findings were reported by Welch and colleagues [17] for both as-cast and HIPed samples from the TaTiCr MPE system.

Additionally, comparing Fig. 1c and d, there is a difference between the phase fractions. Butler and colleagues [16] analyzed the phase transformation of TiNbCr

MPE alloy by CAPHALD methodology using the Nb database in Pandat software. These researchers observed that by increasing the temperature, the BCC fraction also increases. Indeed, the XRD spectra in Fig. 1c and d show a difference between the as-cast and HIPed alloys, most likely due to differences in the thermal processing temperatures. Butler and colleagues [16] also reported that, when comparing the microstructure of the TiNbCr MPE alloy with the NbCr alloy, there is a reversal in the microstructural pattern. While the binary alloy consists of a Laves matrix with BCC precipitates—comprising coarse, near-spherical primary particles and fine lamellae—the introduction of Ti facilitates the formation of an alloy with a BCC matrix containing Laves phase precipitates. The rise in the BCC volume fraction is attributed to a decline in the fraction of the eutectic constituent. This reduction is influenced by the amount of Cr in the alloy and its solubility in the BCC phase, thereby affecting the volume fraction of the Laves phase.

Figures 8 and 9 show that the oxide scale exhibits a different morphology and composition depending on the exposure temperature, suggesting different oxidation mechanisms. While at 800 °C the scale is composed of a mixture of Nb, Ti and Cr oxides with stratified porosity (Fig. 11), an increase in the exposure temperature to 900 and 1000 °C resulted in the clear establishment of an inner Cr₂O₃ layer (Figs. 12 and 13).

Stringer [10] reported the oxidation behavior of pure Nb which scales according to linear kinetics and the scale morphology is similar to that formed on the TiNbCr MPE alloy at 800 °C, i.e., stratified porosity. According to that study, the stratified porosity occurs at temperatures greater than or equal to 800 °C and forms by a sequential vacancy supersaturation mechanism. Specifically, during the oxidation process, a compact Nb₂O₅ scale forms and then grows predominantly by the outward substitutional diffusion of Nb. This outward Nb cation diffusion is balanced by the inward diffusion of vacancies that are injected at the metal/scale interface. In the absence of further migration into the metal, vacancy supersaturation eventually occurs to result in the formation of free space at the metal/scale interface until the supersaturation has been removed. This process of vacancy supersaturation and condensation (i.e., free space formation) is repeated throughout the scale-growth process to result in the appearance of stratified porosity throughout the scale [10]. Important to this mechanism is the rapid growth rate of the Nb₂O₅ scale coupled with vacancy condensation favored at the metal/scale interface.

According to Jiang et al. [9], the interaction between Nb and Ti during oxidation is directly related to the Nb fraction in the alloy. These researchers studied the influence of Nb addition on oxidation behavior of Ti-(0–50 at.%) Al alloys in air at 900 °C up to 24 h. They reported that the scaling kinetics were parabolic up to 20 at.% of Nb addition, after which the kinetics transitioned to linear. It was inferred that for up to 15 at.% Nb addition, the Nb exists as a solid solution with TiO₂. Beyond this Nb level the complex oxide TiNb₂O₇ is stable to form. An increase in the scaling kinetics is in conjunction with the spinel formation until eventually linear growth of a stratified porous scale structure is observed. Comparing the oxidation kinetics of TiNbCr MPE alloy, Table 3, with pure Nb at 800 °C ($k_{\text{Nb}} \sim 9.4 \times 10^{-6} \text{ g/cm}^2 \text{ s}$) [21], it is noted that the former exhibits a slower rate, suggesting that a scale containing the complex oxides composed of Nb and Ti is more protective than pure

Nb_2O_5 . This agrees with the findings of Gorr et al. [8], but it doesn't diminish the inference that the linear scaling kinetics of the TiNbCr MPE alloy is nonprotective.

Increasing the oxidation temperature to 900 and 1000 °C resulted in the formation of an inner Cr_2O_3 layer in the scale on the TiNbCr MPE alloy and a kinetics inversion (i.e., scale growth rate drops with an increase in exposure temperature above 800 °C). The oxidation process of chromium or chromium-alloys is marked by the development of a compact and protective chromium-oxide layer, primarily composed of Cr_2O_3 . This layer acts as a barrier, isolating the metal from the oxidizing environment. The scaling kinetics are typically parabolic [22]. However, at temperatures higher than 1000 °C, the volatilization of Cr_2O_3 is reported, leading to a subsequent decrease in oxidation resistance.

According to Butler et al. [15], when they compared the oxidation behavior of NbCr and the TiNbCr MPE alloy, the inner Cr_2O_3 layer offers some protection, especially at high temperatures (greater than 1000 °C), because the outer scale product rich in TiO_2 can protect against Cr_2O_3 volatilization, thus resulting in an increase in protection. The establishment of a continuous inner Cr_2O_3 layer would be expected to lower the chemical potential of oxygen at the alloy/scale interface, which, in turn, would reduce the extent of oxygen diffusion into the alloy.

The results show that a higher exposure temperature kinetically favors the establishment of an inner Cr_2O_3 scale layer. The same trend was reported by Welch et al. [17] for the TaTiCr MPE system. Thus, it is reasonable to conclude that oxidation at relatively low temperatures (below about 900 °C) should be considered a harsher test for refractory-metal MPE alloys than exposures at higher temperatures. This is noteworthy, since a review of the literature reveals that little attention has been given to the low-temperature oxidation testing of these alloys.

The nonprotective nature of the outer scale formed on the TiNbCr MPE alloy—regardless of whether an inner Cr_2O_3 layer can establish—can enable the formation of oxides and nitrides inside of the alloy. Butler and colleagues [15] showed that a HIPed TiNbCr MPE alloy oxidized at 1200 °C in air for 8 h forms internal oxides and nitrides. They highlighted that the BCC matrix has the favorable formation of $\text{Cr}_3\text{Nb}_3\text{N}$, TiO_2 , small pockets of Nb_2O_3 and highly faceted TiN precipitates. At the same time, the Laves phase forms $\text{Cr}_3\text{Nb}_3\text{N}$, TiO_2 and Cr_2O_3 . The differences in the oxidation behavior of the two phases provide insight to the differences in oxidation behavior between the cast and HIPed TiNbCr MPE systems found in this study. To that end, Fig. 1 shows that the cast alloy has thinner Laves precipitates and also a smaller Laves phase fraction than the HIPed alloy. Gesmundo and Gleeson [25] showed that in the case of two-phase alloys, protective oxide scale formation is more difficult if the precipitates do not have a homogeneous distribution and/or if the oxidation kinetics of the matrix phase is high. Additionally, the ratio of precipitate volume fraction to size must exceed a critical value to have the exclusive formation of the solute-metal oxide on the two-phase alloy, which means that a decrease in the precipitate sizes may help to form a protective scale composed by the solute, in this case Cr [26].

Since the oxidation protection of the TiNbCr MPE alloy occurs due to the Cr oxidation, it is postulated that because the cast alloy has a smaller size distribution of Laves phase than the HIPed version, the Cr_2O_3 formation is promoted to a greater

extent on the former, resulting in slower oxidation kinetics (Fig. 16). Furthermore, the smaller Laves phase fraction indicates a greater amount of chromium is available in the BCC matrix. The simpler structure of the BCC matrix facilitates the outward diffusion of chromium, leading to the formation of Cr_2O_3 and resulting in a decrease in kinetics.

Analyzing the measured time exponents, at 900 °C there is an apparent transition mixed-mode behavior. Based on EDS analysis, Cr_2O_3 layers start to form, indicating that Cr becomes a competing factor with the Nb. The kinetics of the HIPed condition slow down compared to the as-cast condition.

Finally, Figs. 11, 12 and 13 suggest that the two phases presented in the TiNbCr MPE alloy oxidize cooperatively to form a uniform scale due to the constant alloy morphology along the exposure time and a scale composed by continuous layers in composition. This is in agreement with a mechanism described by Gesmundo and Gleeson [25].

Conclusions

This paper represents one of the first steps in the investigation of the oxidation behavior of a TiNbCr MPE alloy at intermediate temperatures. Tests were conducted in air at 800, 900 and 1000 °C up to 100 h. The following key points can be made:

- (1) The microstructure of TiNbCr MPE alloy is composed of a Nb, Ti-rich BCC matrix with Cr-rich Laves phase and, due to the high temperature applied during the HIP process, the Laves phase fraction increased and the precipitate size was larger.
- (2) For all the temperatures tested, the oxidation kinetics of TiNbCr MPE alloy can be described as linear, exhibiting the formation of a nonprotective, stratified porous layer which allows gas ingress through the scale and the formation on an internal reaction zone comprised of oxides and nitrides.
- (3) The oxidation behavior of TiNbCr MPE alloy at 800 °C differs from that at 900–1000 °C. At 800 °C, the scale is composed of a mixture of Nb, Ti and Cr with no defined layer, exhibiting a morphology close to Nb oxidation. In this condition, the as-cast MPE exhibited better behavior; however, as the temperature increased, the establishment of an inner Cr_2O_3 layer decreased the oxidation rate, shifting the favorable behavior to the HIPed condition.
- (4) Cyclic testing results were found to be similar to those of isothermal testing from the standpoint of kinetics, but the former did result in more scale damage and consequently differences in scale microstructure.

Acknowledgements This study was financed in part by the Coordenação de Aperfeiçoamento de Pessoal de Nível Superior—Brasil (CAPES)—Finance Code 001. Work by I. Dainezi was financially supported through CAPES/PrInt—Coordenação de Aperfeiçoamento de Pessoal de Nível Superior/Programa Institucional de Internacionalização process n° 88887.696560/2022-00 and CAPES—Coordenação de Aperfeiçoamento de Pessoal de Nível Superior process n° 88887.500991/2020-00. Technical and financial support from the University of Pittsburgh. Dr. Butler from the Air Force Research Lab for his work

on casting and HIPing in its HIPed condition and his availability to discuss analysis. Dr. Nunes and his research group from the DEMAEEEL—USP (University of São Paulo) for their work on casting the TiNbCr alloy in its as-cast condition. PPGCEM/UFSCar (Graduate Program in Materials Science and Engineering/Federal University of São Carlos), the Brazilian research-funding agencies CNPq (National Council for Scientific and Technological Development – grant no. 406740/2021-6, 407624/2022-8, 315903/2023-6) and FAPESP (São Paulo Research Foundation – grant no. 2022/03139–9) for their financial support to this work.

Author Contributions Isabela Dainezi contributed to conceptualization, methodology, formal analysis, investigation, data curation and writing—original draft, review and editing; Brian Gleeson contributed to conceptualization, methodology, formal analysis, investigation, data curation, supervision, funding acquisition, resources and writing—review and editing; Bruno Resende Buzatti contributed to methodology, formal analysis, investigation and data curation; Artur Mariano de Sousa Malafaia contributed to methodology, formal analysis, investigation, data curation and writing—review and editing; Carlos Alberto Della Rovere contributed to conceptualization, formal analysis, supervision, project administration, funding acquisition, resources and writing—review and editing.

Declarations

Conflict of interest The authors declare that they have no known competing financial interests or personal relationships that could have appeared to influence the work reported in this paper.

References

1. N. Birbilis, S. Choudhary, J. R. Scully, and M. L. Taheri, *npj Materials Degradation* **5**, 2021 (1).
2. D. B. Miracle and O. N. Senkov, *Acta Materialia* **122**, 2017 (448).
3. B. Cantor, *Entropy* **16**, 2014 (4749).
4. E. P. George, D. Raabe, and R. O. Ritchie, *Nature Reviews Materials* **4**, 2019 (515).
5. H. Shi, C. Tang, A. Jianu, R. Fetzer, A. Weisenburger, M. Steinbrueck, M. Grosse, R. Stieglitz, and G. Müller, *Corrosion Science* **170**, 2020 (108654).
6. K. Chattopadhyay, R. Mitra, and K. K. Ray, *Metallurgical and Materials Transactions A* **39**, 2008 (577).
7. B. Gorr, F. Mueller, H. J. Christ, T. Mueller, H. Chen, A. Kauffmann, and M. Heilmaier, *Journal of Alloys and Compounds* **688**, 2016 (468).
8. B. Gorr, S. Schellert, F. Müller, H. J. Christ, A. Kauffmann, and M. Heilmaier, *Advanced Engineering Materials* **23**, 2021 (1).
9. H. Jiang, M. Hirohasi, Y. Lu, and H. Imanari, *Scripta Materialia* **46**, 2002 (639).
10. J. Stringer, *Acta Metallurgica* **17**, 1969 (1227).
11. O. N. Senkov, D. B. Miracle, K. J. Chaput, and J. P. Couzinie, *Journal of Materials Research* **33**, 2018 (3092).
12. N. R. Phillips, M. Carl, and N. J. Cunningham, *Metallurgical and Materials Transactions A* **51**, 2020 (3299).
13. O. Kubaschewski and B. E. Hopkins, *Journal of the Less Common Metals* **2**, 1960 (172).
14. J. Hidde, C. Gugushev, and D. Klimm, *Journal of Crystal Growth* **509**, 2019 (60).
15. T. M. Butler, O. N. Senkov, T. I. Daboiku, M. A. Velez, H. E. Schroader, L. G. Ware, and M. S. Titus, *Intermetallics* **140**, 2022 (07374).
16. T. M. Butler, O. N. Senkov, M. A. Velez, and T. I. Daboiku, *Intermetallics* **138**, 2021 (107323).
17. N. J. Welch, M. J. Quintana, T. M. Butler, and P. C. Collins, *Journal of Alloys and Compounds* **941**, 2023 (169000).
18. HAYNES® 188® alloy. Nominal Composition. (n.d.). <https://www.haynesintl.com/en/datasheet/haynes-188-alloy/#nominal-composition>
19. R. B. Herchenroeder and H. A. No, *188 Aging Characteristics*. International symposium on structural stability in superalloys, (1968), p. 110.
20. V. P. Deodshumukh, S. K. Srivastava, and J. Bai, *Materials and Corrosion* **64**, 2013 (772).
21. J. T. Clenny and C. J. Rosa, *Metallurgical Transactions A* **11**, 1980 (1385).

22. K. P. Lillerud and P. Kofstad, *Journal of the Electrochemical Society* **127**, 1980 (2397).
23. P. Kofstad and K. P. Lillerud, *Journal of the Electrochemical Society* **127**, 1980 (2410).
24. H. C. Graham and H. H. Davis, *Journal of the American Ceramic Society* **54**, 1971 (89).
25. F. Gesmundo and B. Gleeson, *Oxidation of Metals* **44**, 1995 (211).
26. G. Wang, B. Gleeson, and D. L. Douglass, *Oxidation of Metals* **35**, 1991 (317).

Publisher's Note Springer Nature remains neutral with regard to jurisdictional claims in published maps and institutional affiliations.

Springer Nature or its licensor (e.g. a society or other partner) holds exclusive rights to this article under a publishing agreement with the author(s) or other rightsholder(s); author self-archiving of the accepted manuscript version of this article is solely governed by the terms of such publishing agreement and applicable law.